CHEMISTRY OF MATERIALS

pubs.acs.org/cm

Article

$Ba_4RuMn_2O_{10}$: A Noncentrosymmetric Polar Crystal Structure with Disordered Trimers

Callista M. Skaggs, Peter E. Siegfried, Jun Sang Cho, Yan Xin, V. Ovidiu Garlea, Keith M. Taddei, Hari Bhandari, Mark Croft, Nirmal J. Ghimire, Joon I. Jang, and Xiaoyan Tan*

Cite This: *Chem. Mater.* 2024, 36, 6053−6061

Read Online

ACCESS | Metrics & More | Article Recommendations | Supporting Information

ABSTRACT: Phase-pure polycrystalline $Ba_4RuMn_2O_{10}$ was prepared and determined to adopt the noncentrosymmetric polar crystal structure (space group $Cmc2_1$) based on results of second harmonic generation, convergent beam electron diffraction, and Rietveld refinements using powder neutron diffraction data. The crystal structure features zigzag chains of corner-shared trimers, which contain three distorted face-sharing octahedra. The three metal sites in the trimers are occupied by disordered Ru/Mn with three different ratios: Ru1:Mn1 = 0.202(8):0.798(8), Ru2:Mn2 = 0.27(1):0.73(1), and Ru3:Mn3 = 0.40(1):0.60(1), successfully lowering the symmetry and inducing the polar crystal structure from the centrosymmetric parent compounds $Ba_4T_3O_{10}$ (T = Mn, Ru; space group *Cmca*). The valence state of Ru/Mn is confirmed to be +4 according to X-ray absorption near-edge spectroscopy. $Ba_4RuMn_2O_{10}$ is a narrow bandgap (∼0.6 eV) semiconductor exhibiting spin-glass behavior with strong magnetic frustration and antiferromagnetic interactions.

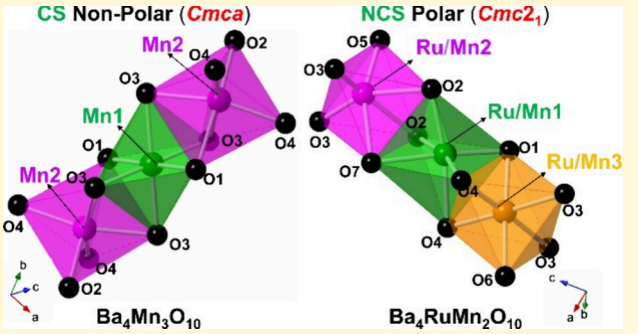

INTRODUCTION

Inorganic materials lacking inversion symmetry are defined as noncentrosymmetric (NCS) materials. A subgroup of NCS crystal structures containing a polar axis is categorized into the NCS polar crystal structure system, which can be simplified as polar materials.[1] Such materials can be used in laser technology, access memory elements, energy conversion, and spintronics.[1−4] Currently, it is still very challenging to predict and design novel polar materials based on very limited design strategies.[5−7] Converting centrosymmetric (CS) compounds into NCS polar materials is an alternative way to achieve polar materials, considering the existence of more CS than NCS materials.[8] The CS to NCS polar structural transition could happen within a compound as temperature changes, as shown in conventional insulating ferroelectrics. Such ferroelectric-like transitions have also been reported in metallic compounds (e.g., $LiOsO_3$), known as interesting "ferroelectric metals", which have drawn intensive attention in recent years.[9] We are therefore inspired to achieve NCS polar compounds based CS compounds via small modifications.

Here, we report an interesting example of obtaining NCS polar compounds based on CS parent compounds $Ba_4T_3O_{10}$ (T = Mn, Ru). $Ba_4T_3O_{10}$ (T = Mn, Ru) fit in the general formula $A_{n+1}T_nO_{3n+1}$ (A = Ca, Sr, Ba, T = transition metals) typically used for representing the Ruddlesden−Popper (R−P) phase. Normal R−P phase crystallizes in the CS space group $I4/mmm$ featuring corner-sharing octahedra,[10] while $Ba_4T_3O_{10}$ (T = Mn, Ru) adopts a different CS crystal structure (space group *Cmca*) with zigzag chains of corner-shared trimers (T_3O_{12}) containing face-sharing octahedra (Figure 1a).[11−13] In each trimer, the middle distorted TO_6 octahedron is symmetrically connected to two identical distorted TO_6 octahedra, corresponding to the two T sites in the crystal structure. It recently came to our attention that CS $Ba_4T_3O_{10}$ (T = Mn, Ru) can be induced to NCS polar compounds by creating three uneven distortions in the trimers, which will promote symmetry breaking to generate a polar crystal structure with three distinct metal sites, lowering the symmetry to $Cmc2_1$ (a subgroup of the parent *Cmca* space group).[14] A previous single-crystal X-ray study of $Ba_4Ru_{1.1}Mn_{1.9}O_{10}$ indicates that it crystallizes in the polar space group $Cmc2_1$, with three disordered Ru/Mn sites with different ratios of Ru:Mn on each site (Figure 1b).[15]

To date, the phase-pure polycrystalline sample of $Ba_4Ru_{1.1}Mn_{1.9}O_{10}$ has not been reported, and there has been no detailed study to confirm the polar crystal structure via other techniques and to investigate its unknown physical

Received: February 29, 2024
Revised: May 6, 2024
Accepted: May 22, 2024
Published: June 11, 2024

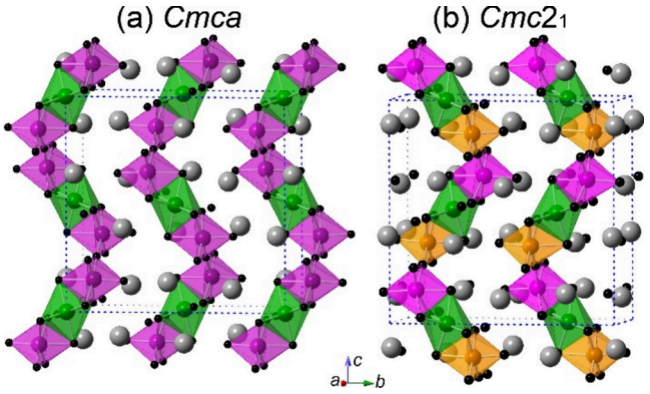

Figure 1. Crystal structure of (a) $Ba_4T_3O_{10}$ (T = Mn, Ru) and (b) $Ba_4RuMn_2O_{10}$. Color code: Ba = gray, O = black, T1 = green, T2 = purple in (a), Ru/Mn1 = green, Ru/Mn2 = purple, Ru/Mn3 = orange in (b).

properties further. In this study, we report the synthesis of $Ba_4Ru_{1.1}Mn_{1.9}O_{10}$ and the determination of the NCS polar crystal structure with second harmonic generation, convergent beam electron diffraction, and neutron powder diffraction. The oxidation state of transition metals will be revealed with X-ray absorption near-edge spectroscopy. We also report the magnetic and resistivity properties.

EXPERIMENTAL SECTION

Starting Materials and Synthesis. Polycrystalline samples of $Ba_4RuMn_2O_{10}$ were synthesized through a two-step solid-state process. $BaCO_3$ (99.997% mass fraction, Alfa Aesar), RuO_2 (99.95% mass fraction, Alfa Aesar), and MnO_2 (99.997% mass fraction, Alfa Aesar) were used as precursors. The precursors were mixed in a stoichiometric ratio and thoroughly ground in an argon-filled glovebox with a low concentration of O_2 and H_2O (<1 ppm). The mixtures were pressed into a 6 mm pellet (<3 tons). The pellet was then placed in an alumina crucible which was heated to 1000 °C in a box furnace over 12 h, retained at the same temperature for 48 h, and cooled to room temperature as the furnace cooled naturally. The obtained sample was then thoroughly ground in air and repressed into a 6 mm pellet (<3 tons), which was heated to 1350 °C over 12 h, held at 1350 °C for 72 h, and cooled to room temperature with furnace cooling. During the sample preparation, no uncommon hazards were noted.

Powder X-ray and Neutron Diffraction. Powder X-ray diffraction (PXRD) patterns of polycrystalline samples were obtained at room temperature with a scattering angle 2θ ranging from 10° to 70° for 30 min using a benchtop Miniflex-600 powder X-ray diffractometer (Cu Kα, λ = 1.5418 Å). Powder neutron diffraction (PND) data were obtained at the HB-2A (λ = 1.5398 Å) beamline at the High Flux Isotope Reactor at the Oak Ridge National Laboratory.[16,17] About 3 g of polycrystalline powders were loaded in a vanadium sample holder (inner diameter = 6 mm), and data were collected between 1.7 and 250 K. Rietveld refinements were performed using the FullProf suite of programs.[18]

Second Harmonic Generation (SHG). Microcrystalline powders of $Ba_4RuMn_2O_{10}$ were sealed in a glass capillary tube and mounted on a homemade sample holder for SHG measurement. Excitation was achieved using an ultrafast Ti:sapphire laser with a pulse width of 100 fs and a repetition rate of 80 MHz, operating at an input wavelength (λ) of 800 nm. The laser beam was focused onto the sample using a lens with a focal length of 75 mm. The signal, with a wavelength (λ_{SHG}) of $\lambda/2$ (400 nm), was collected under a reflection geometry by using a fiber-optic bundle coupled to a high-resolution spectrometer, which then directed the signal to a charge-coupled device camera. A long data collection time of 10 min was required to obtain the SHG signal well above the signal-to-noise level.

Chemical Analysis. Elemental analysis of polycrystalline samples of $Ba_4RuMn_2O_{10}$ was carried out using a JEOL scanning electron microscope (SEM), JSM-IT500HRLV SEM, and the attached Octane Elect Plus energy dispersive X-ray spectroscopy (EDX) system. The SEM images were collected with an accelerating voltage of 15 kV.

Transmission Electron Microscopy (TEM). TEM data were collected on a probe aberration-corrected subangstrom resolution JEOL JEM-ARM200cF microscope at 200 kV. Electron-transparent thin pieces used in the TEM experiments were prepared from crushed polycrystalline powders, which were transferred onto a carbon-coated 200-mesh Cu TEM grid. Selected-area electron diffraction patterns were collected from single thin pieces. Atomic resolution high-angle annular dark-field scanning transmission electron microscopy (HAADF-STEM) images were also obtained using a probe of 0.078 nm with a convergent angle of 21 mrad and an inner collection angle of 74 mrad. Convergent beam electron diffraction (CBED) patterns were obtained by focusing the electron beam onto the sample surface into a 10 nm diameter area in TEM mode.

X-ray Absorption Near-Edge Spectroscopy (XANES). The Ru-L_3 XANES data were collected in total electron yield mode with sequential standards at the National Synchrotron Light Source II (NSLS-II) insertion device beamline 7-ID-2 SST-2 using a Si-111 monochromator, Brookhaven National Laboratory. The Mn-K and Ru-K edge data were collected in both the transmission and fluorescence mode with simultaneous standards at NSLS-II beamline 7BM QAS using a channel cut Si-111 monochromator. Standard spectra were taken on NSLS-I X-19A using a Si-111 double-crystal monochromator.

Physical Properties. The ACMS II option in a Quantum Design Dynacool physical property measurement system (PPMS) and the MMPS system in the superconducting quantum interference device (SQUID) magnetometer were used to measure the magnetic properties of a polycrystalline sample of $Ba_4Mn_2RuO_{10}$. Magnetic susceptibility measurements with zero-field-cooled (ZFC) and field-cooled (FC) modes were recorded between 400 and 1.8 K in a magnetic field of 0.1 and 0.2 T. Field-dependent magnetizations were measured from −9 to 9 T at 2, 10, 50, 100, 200, and 300 K. AC magnetic susceptibility measurements were performed between 1.8 and 25 K with four different frequencies (1, 10, 100, and 1000 Hz) under 0 T. Heat capacity measurements were conducted on a dense pellet of $Ba_4RuMn_2O_{10}$ from 1.8 to 50 K under 0 T using PPMS. Resistivity measurement was conducted on a pellet (74% density, diameter = 13 mm) from 300 to 1373 K with the four-probe method using the NETZSCH SBA 458 Nemesis system.

RESULTS AND DISCUSSION

Synthesis and PXRD. The polycrystalline $Ba_4RuMn_2O_{10}$ powders were prepared using a two-step solid-state method with starting materials $BaCO_3$, RuO_2, and MnO_2 based on a heating profile of $Ba_4Mn_3O_{10}$.[19] The obtained sample was initially checked with a laboratory PXRD technique (Figure 2). The experimental PXRD pattern was compared to the theoretical patterns of $Ba_4RuMn_2O_{10}$ (space group $Cmc2_1$) and parent $Ba_4Ru_3O_{10}$ (space group $Cmca$). A calculated pattern of $Ba_4RuMn_2O_{10}$ with space group $Cmca$ was also simulated based on the structure model of $Ba_4Ru_3O_{10}$ with two metal sites via fixing the ratios of Ru:Mn to be 1:2. As shown in Figure S1, three reflections ((020, (021), and (112)) shown at low angles are similar in both theoretical patterns of $Ba_4RuMn_2O_{10}$, with a small difference in the intensity of the (020) and (021) reflections. The pattern of $Ba_4Ru_3O_{10}$ shows a (111) reflection at low angles, which is not observable in those of $Ba_4RuMn_2O_{10}$ but displays a very low intensity of (112) reflection. Our experimental PXRD matches better with the previously reported polar crystal structure with the space group $Cmc2_1$.

https://doi.org/10.1021/acs.chemmater.4c00586
Chem. Mater. 2024, 36, 6053−6061

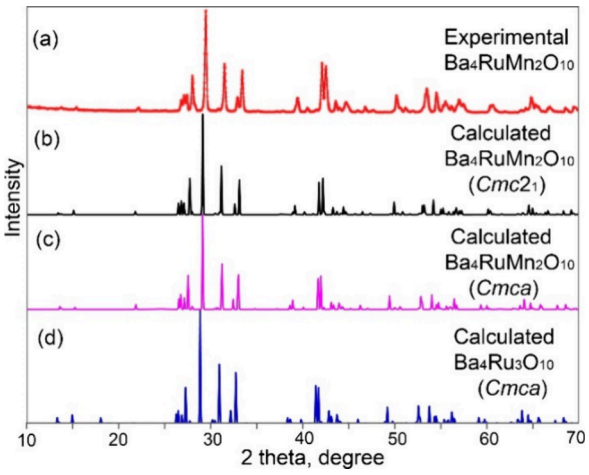

Figure 2. PXRD pattern of $Ba_4RuMn_2O_{10}$ (a) compared with calculated patterns of $Ba_4RuMn_2O_{10}$ with the space groups *Cmc*2$_1$ (b) and *Cmca* (c) and that of $Ba_4Ru_3O_{10}$ with the space group *Cmca* (d).

SHG. To confirm the NCS nature of the crystal structure, an SHG measurement was performed on microcrystalline powders of $Ba_4RuMn_2O_{10}$. With an input laser source wavelength (λ) of 800 nm, the SHG signal is observed at a wavelength (λ_{SHG}) of $\lambda/2$ (400 nm) (Figure 3). The SHG is

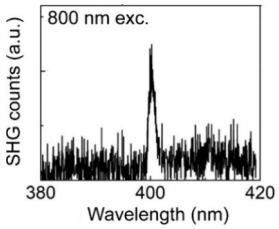

Figure 3. SHG spectrum observed from $Ba_4RuMn_2O_{10}$.

relatively weak due to the significant absorption of SHG light by the sample itself, considering that the corresponding SHG photon energy (~3.1 eV) is much higher than the bandgap (~0.6 eV, as shown below) of $Ba_4RuMn_2O_{10}$. The data were carefully collected to ensure that the signal was well above the signal-to-noise level. The SHG signal was confirmed to be intrinsic to the sample, unambiguously demonstrating the NCS nature of $Ba_4RuMn_2O_{10}$.

TEM. To confirm the polar space group (*Cmc*2$_1$) of $Ba_4RuMn_2O_{10}$, a room-temperature TEM experiment was performed. The CBED pattern is able to distinguish 32 point groups due to dynamic scattering.[20] The space group *Cmca* has point group *mmm*, while space group *Cmc*2$_1$ has point group *mm*2, but both have the same Laue class *mmm*. To distinguish the point group, we tilted the single thin piece to the [010] zone axis and acquired a whole CBED pattern at a low camera length (Figure 4a). For the [010] zone axis, the whole CBED pattern should have 2*mm* symmetry for the point group *mmm* (space group *Cmca*) and one mirror symmetry *m* for the point group *mm*2 (space group *Cmc*2$_1$). There is only one mirror plane symmetry *m* for the whole pattern in Figure 4a, confirming that $Ba_4RuMn_2O_{10}$ adopts the polar space group *Cmc*2$_1$.

The projected atomic structure of the thin piece along the [110] direction is revealed by an atomic resolution high-angle annular dark-field scanning TEM (HAADF-STEM) image

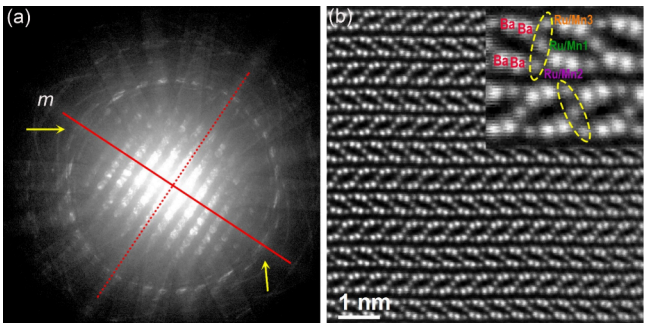

Figure 4. (a) CBED whole pattern along the [010] zone axis. The guiding line for the mirror plane is the solid red line, while the dotted line indicates another possible mirror plane position. The diffraction features that the yellow arrows pointed to are not the same, confirming the nonexistence of a second mirror plane. (b) Atomic resolution HAADF-STEM image of the thin piece along [110] and an enlarged section of HAADF-STEM image (inset) of $Ba_4RuMn_2O_{10}$.

(Figure 4b). The intensity of white dots are projected atomic columns in Figure 4b, and they are proportional to the square of atomic number (Z^2) of atoms.[21] The pairs of intense white dots correspond to two Ba atoms, and the three darker dots between these brighter pairs are projected as three disordered Ru/Mn columns. O atoms (too low *Z*) are not visible in the image. The quantitatively measured intensity for each Ru/Mn column in the HAADF-STEM image is different, suggesting that all three positions are disordered with different ratios of Ru:Mn.

PND. To further understand the disordered metal sites in the crystal structure, Rietveld refinements were performed using PND data collected at 250 K. The reported crystal structure defined by the space group *Cmc*2$_1$ was used as the starting model for Rietveld refinements, which reproduced the experimental PND pattern very well (Figure 5). Selected

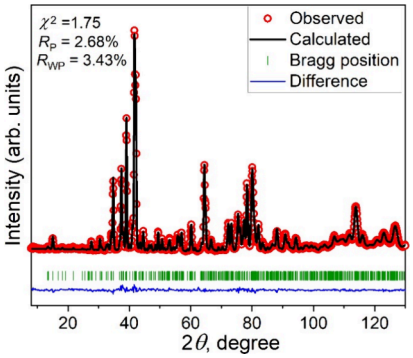

Figure 5. Rietveld refinement of $Ba_4RuMn_2O_{10}$ in the space group *Cmc*2$_1$ using PND data. The observed data (red), calculated pattern (black), and the difference between those two patterns (blue) are provided.

refined structural parameters are listed in Table 1. The refined unit cell parameters are a = 5.7440(1) Å, b = 13.1747(3) Å, c = 12.8957(2) Å, and V = 975.88(3) Å^3, which are close to the reported values a = 5.735(3) Å, b = 13.148(4) Å, c = 12.855(8) Å, and V = 969.3 (8) Å^3.[4] The three transition metal sites (T1, T2, and T3) were refined independently with the refined ratios of Ru1:Mn1 = 0.202(8):0.798(8), Ru2:Mn2 = 0.27(1):0.73(1), and Ru3:Mn3 = 0.40(1):0.60(1), which are slightly different from the reported ratios with Ru1:Mn1 =

https://doi.org/10.1021/acs.chemmater.4c00586
Chem. Mater. 2024, 36, 6053−6061

Table 1. Selected Structure Parameters of Rietveld Refinement Details of $Ba_4RuMn_2O_{10}$ Using PND Data

sample	$Ba_4RuMn_2O_{10}$
empirical formula	$Ba_4Ru0.87(2)Mn2.13(2)O_{10}$
temperature, K	250
mol wt, g/mol	914.25
density (calculated), g/cm^3	6.225
neutron wavelength (λ), Å	1.5398
space group, #	$Cmc2_1$, #36
Z	4
lattice parameters	a = 5.7440(1) Å, b = 13.1747(3) Å, c = 12.8957(2) Å, V = 975.88(3) Å^3
Rietveld criteria of fit	R_p = 2.68%, R_{wp} = 3.43%, R_{Bragg} = 3.44%, χ^2 = 1.75

site	Wyckoff symbol	x, y, z	occ
Ba1	4a	0, 0.006(1), 0.907(2)	1
Ba2	4a	0, 0.717(2), 0.869(2)	1
Ba3	4a	0, 0.214(1), 0.649(2)	1
Ba4	4a	0, 0.511(1), 0.624(2)	1
Ru1/Mn1	4a	0, 0.240(3), 0	0.202(8)/0.798(8)
Ru2/Mn2	4a	0, 0.882(5), 0.678(5)	0.27(1)/0.73(1)
Ru3/Mn3	4a	0, 0.362(7), 0.867(3)	0.40(1)/0.60(1)
O1	4a	0, 0.215(1), 0.864(2)	1
O2	8b	0.224(1), 0.1470(8), 0.047(2)	1
O3	8b	0.253(3), 0.3692(3), 0.756(2)	1
O4	8b	0.221(2), 0.3564(8), 0.975(2)	1
O5	4a	0, 0.0148(1), 0.649(2)	1
O6	4a	0.5, 0.015(1), 0.860(2)	1
O7	4a	0.5, 0.220(1), 0.655(2)	1

0.15:0.85, Ru2:Mn2 = 0.325:0.675, and Ru3:Mn3 = 0.6:0.4. Our refined total ratio of Ru:Mn is 0.87:2.13, which is smaller than that of the previously reported $Ba_4Ru_{1.1}Mn_{1.9}O_{10}$. This discrepancy can be attributed to small sample differences and data collection of different diffraction techniques, PND vs single-crystal X-ray diffraction. We consider that neutron diffraction offers much better sensitivity to the Ru/Mn atomic ratio due to the large contrast in coherent scattering lengths of Mn (−3.73 fm) and Ru (7.03 fm). To verify the robustness of our reported values, we repeated our Rietveld refinements by varying the number of parameters and also by applying different constraints or restraints to the site occupancies. All refinements produced similar atomic occupancies with Ru:Mn = 0.87:2.1. The chemical analysis using the SEM-EDX technique indicates the ratio of Ba:Ru:Mn:O = 4.1:0.8:1.9:10 (Figure S2), which is close to the ratio of the title compound. For the purpose of simplicity, the nominal composition $Ba_4RuMn_2O_{10}$ will be used in the following discussion.

The refined Mn/Ru−O bond distances (d) vary from 1.79(3) to 2.15(7) Å (Table 2), which are close to those (1.83−2.14 Å) in $Ba_4Ru_{1.1}Mn_{1.9}O_{10}$,[15] the Ru−O bond distances (1.92−2.12 Å) in $Ba_4Ru_3O_{10}$,[22] and the Mn−O bond distances (1.81−2.09 Å) in $Ba_4Mn_3O_{10}$.[12] Figure 6 shows

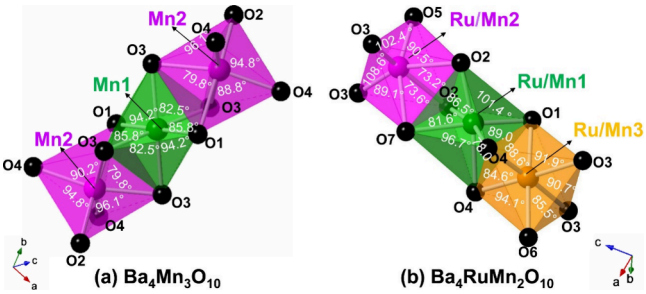

Figure 6. A zoomed-in trimer in the crystal structure of (a) $Ba_4Mn_3O_{10}$ (space group $Cmca$) and (b) $Ba_4RuMn_2O_{10}$ (space group $Cmc2_1$). Color code: Ru/Mn1 = green, Ru/Mn2 = purple, Ru/Mn3 = orange, O = black.

a comparison of a zoomed-in trimer of $Ba_4Mn_3O_{10}$ and $Ba_4RuMn_2O_{10}$. In the trimer of $Ba_4Mn_3O_{10}$ (Figure 6a), the centering $Mn1O_6$ octahedron is more symmetric than the Mn_2O_6 octahedra: Mn1 atom coordinates with four O3 (d = 1.90 Å) and two O1 (d = 1.91 Å), and the angles of O−Mn1−O are 82.5°, 85.8°, and 94.2°, while the Mn2 atom coordinates with two O3 (d = 1.96 Å), two O4 (d = 1.88 Å), and one O2 (d = 1.81 Å) and O1 (d = 2.09 Å), and the angles of O−Mn2−O vary from 79.8° to 96.1°.[12] The trimer of $Ba_4RuMn_2O_{10}$ is more distorted than that of $Ba_4Mn_3O_{10}$ due to a larger difference in bond distances within each octahedron (Table 2), with the ranges of 1.79−2.07, 1.79−2.15, and 1.89−2.04 Å in the $Ru/Mn1O_6$, Ru/Mn_2O_6, and Ru/Mn_3O_6 octahedron, respectively. The angles of the octahedrons of the O−Ru/Mn−O vary in the ranges of 78.0°−101.4°, 73.2°−108.6°, and 85.5°−94.1° in the $Ru/Mn1O_6$, Ru/Mn_2O_6, and Ru/Mn_3O_6 octahedron, respectively (Figure 6b). The $Ru/Mn3O_6$ octahedron is the least distorted and the $Ru/Mn2O_6$ octahedron is the most distorted in the trimer of $Ba_4RuMn_2O_{10}$.

The three partially disordered metal sites in $Ba_4RuMn_2O_{10}$ are different from the totally disordered sites, where two elements are randomly occupied with a ratio of 50:50. Many double perovskite $A_2B'B''O_6$ (A, B = elements as cation ions) form totally disordered sites when the radius difference (Δr) of B′ and B″ ions is within 0.04 Å.[23] The formation of such partially disordered metal sites in $Ba_4RuMn_2O_{10}$ may be related to the large Δr (0.09 Å) between 3d-Mn^{4+} (0.53 Å) and 4d-Ru^{4+} ions (0.62 Å).[24] The designing strategy, creating unevenly disordered sites in trimers via mixing two different transition metal ions with a relatively large Δr, is different from the typical method of stabilizing polar materials with ordered cation ions, e.g., $A_2B'B''O_6$,[25−29] $Ba_4RuTi_2O_9$,[30,31]

Table 2. Selected Bond Distances in $Ba_4RuMn_2O_{10}$

Ru/Mn1−O distances (Å)		Ru/Mn2−O distances (Å)		Ru/Mn3−O distances (Å)	
Ru/Mn1−O1	1.79(3)	Ru/Mn2−O5	1.79(7)	Ru/Mn3−O4	1.89(4) × 2
Ru/Mn1−O2	1.88(3) × 2	Ru/Mn2−O3	1.75(5) × 2	Ru/Mn3−O6	2.02(9)
Ru/Mn1−O4	2.02(3) × 2	Ru/Mn2−O2	2.16(6) × 2	Ru/Mn3−O1	1.94(9)
Ru/Mn1−O7	2.07(3)	Ru/Mn2−O7	2.15(7)	Ru/Mn3−O3	2.04(4) × 2

https://doi.org/10.1021/acs.chemmater.4c00586
Chem. Mater. 2024, 36, 6053−6061

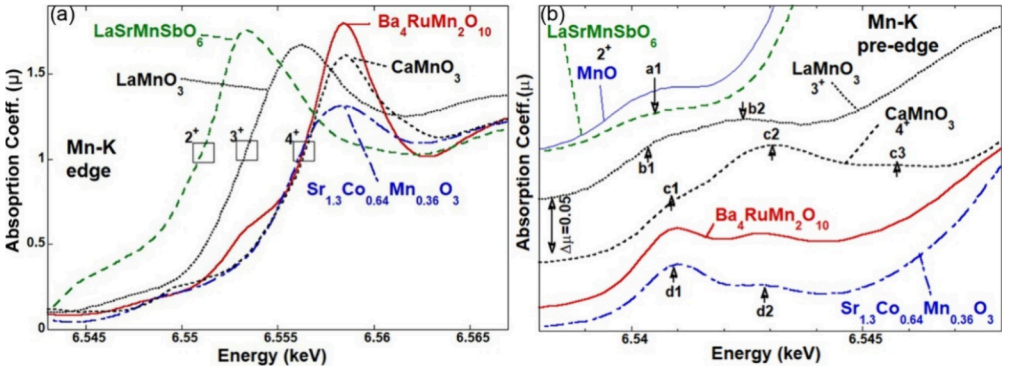

Figure 7. (a) Mn−K edge and (b) pre-edge spectra of $Ba_4RuMn_2O_{10}$ and a series of standard Mn-containing compounds: $LaSrMn^{2+}SbO_6$, $LaMn^{3+}O_3$, and $CaMn^{4+}O_3$.

$Ba_3CuSb_2O_9$,[32] etc. But it is worth noting that polar materials with partially disordered sites have been reported in some hexagonal perovskite-related compounds containing dimers, such as $Ba_3Fe_{1.56}Ir_{1.44}O_9$ ($P3_1mc$)[33] and $Ba_3TiIr_2O_9$ ($P6_3mc$).[34,35] $Ba_4RuMn_2O_{10}$ is an interesting example of converting CS materials with trimers to NCS polar materials.

XANES. Based on the experimental bond distances in Table 2, the bond valence sum (BVS) can be estimated for each site[36] by assuming the T1 = Mn, T2 = Mn, T3 = Ru, and the calculated BVS value for each T site is 3.8, 4.0, and 4.2, respectively, which indicates the oxidation state of +4 for Ru/Mn ions. To further study the valence states of Ru and Mn, XANES measurements were performed to collect the Mn-K, Ru-L_3, and Ru-K edges.

The main edge features at 3*d* transition metal K edges are dominated by 1*s* to 4*p* transition peak features, riding on a step-continuum feature, with a chemical shift to higher energy with increasing valence. In comparison with perovskite-based (corner sharing) $LaSrMn^{2+}SbO_6$, $LaMn^{3+}O_3$, and $CaMn^{4+}O_3$, and face-sharing $Sr_{1.3}Co_{0.64}Mn^{4+}O_3$ standards,[37−39] the chemical shift of the Mn−K edge of $Ba_4RuMn_2O_{10}$ compounds is consistent with a Mn^{4+} valence assignment (Figure 7a). Moreover, the lower energy shoulder in the title compound spectrum (near 6.553 keV) is similar to that of the face-sharing standard spectrum of $Sr_{1.3}Co_{0.64}Mn^{4+}O_3$.[39]

The pre-edge features provide additional insight into the valence state. As shown in Figure 7b, the a1, b1−b2, and c1−c2−c3 features are characteristic of the non-face-sharing Mn^{2+}, Mn^{3+}, and Mn^{4+} in $LaSrMn^{2+}SbO_6$, $LaMn^{3+}O_3$, and $CaMn^{4+}O_3$, respectively. The d1−d2 feature pattern is characteristic of face-sharing Mn^{4+} in the $Sr_{1.3}Co_{0.64}Mn^{4+}O_3$. The pre-edge spectrum of $Ba_4RuMn_2O_{10}$ is consistent with that of $Sr_{1.3}Co_{0.64}Mn^{4+}O_3$ (Figure 7b), which further confirms the face-sharing Mn^{4+} character of this compound.

The Ru-L_3 edge of $Ba_4RuMn_2O_{10}$ is compared with those of the elemental Ru^0, $Ru^{4+}O_2$, and $Ca_2YRu^{5+}O_6$ standards (Figure 8).[40,41] The Ru-L_3 edge is dominated by an intense peak feature due to transitions into empty 4*d* states with the peak structures directly reflecting the 4*d*-orbital crystal field splittings. With increasing valence (decreasing 4*d* count) in the elemental Ru^0-$4d^7$, Ru^{4+}-$4d^4$, and Ru^{5+}-$4d^3$, one can clearly note that the centrum of these 4*d*-features chemically shifts to higher energy, and its intensity increases (due to the presence of additional 4*d* hole states).[40,41] The centrum chemical shift and the spectral intensity (and distribution) of the $Ba_4RuMn_2O_{10}$ Ru-L_3 spectrum evidence its Ru^{4+}-$4d^4$ configuration assignment. This assignment is corroborated by the

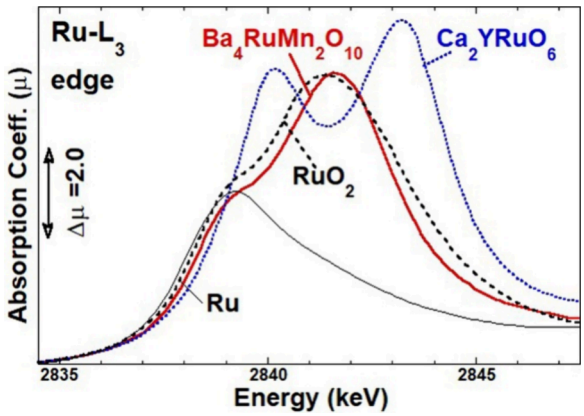

Figure 8. (a) Ru-L_3 edges of $Ba_4RuMn_2O_{10}$ and a set of standard materials: Ru, RuO_2, and Ca_2YRuO_6.

chemical shift of the Ru−K edge of $Ba_4RuMn_2O_{10}$ compared to those of Ru^0, $Ru^{4+}O_2$, $Ca_2YRu^{5+}O_6$, and $Sr_2YRu^{5+}O_6$ in Figure S3.

Physical Properties. The zero-field-cooled and field-cooled (ZFC-FC) magnetic susceptibility data present a cusp near 10 K in the ZFC process, but it keeps increasing in the FC process. The observed divergence between the ZFC and FC data indicates the possible spin-glass behavior (Figure 9). For spin-glass materials, the FC magnetic susceptibility typically saturates due to spin freezing below the defined temperature T_f, the cusp that is more obvious in the ZFC process. In this compound, the FC susceptibility shows behavior similar to that of ZFC when the applied magnetic field is 0.1 T (Figure S4), but it increases obviously below the T_f (10 K) when the magnetic field is increased to 0.2 T, which supports the metastable frozen states in the spin-glass materials. The isothermal field-dependent magnetization data measured at 10 K overlap with those at 2 K, and it slightly deviates from the linear behavior (Figure 9b). The magnetizations measured between 50 and 300 K are linear, as expected. Fitting the inverse FC magnetic susceptibility between 300 and 400 K with the Curie−Weiss law, $\chi = \chi_0 + C/(T - \Theta_w)$, yields the constant diamagnetic term $\chi_0 = -0.0006(2)$ emu/mol and a negative Weiss constant (Θ_w) of −479 K (Figure 9a), which indicates the antiferromagnetic (AFM) interactions. The obtained effective moment (μ_{eff} = 6.89 μ_B/f.u.) given by $\sqrt{8C}$, where *C* is the Curie constant from the Curie−Weiss fitting, is smaller than the expected theoretical value (7.27 μ_B/f.u.) based on $\mu_{eff}^2 = 0.87 \times \mu_{eff}(Ru^{4+})^2 + 2.13 \times \mu_{eff}(Mn^{4+})^2$,

https://doi.org/10.1021/acs.chemmater.4c00586
Chem. Mater. 2024, 36, 6053−6061

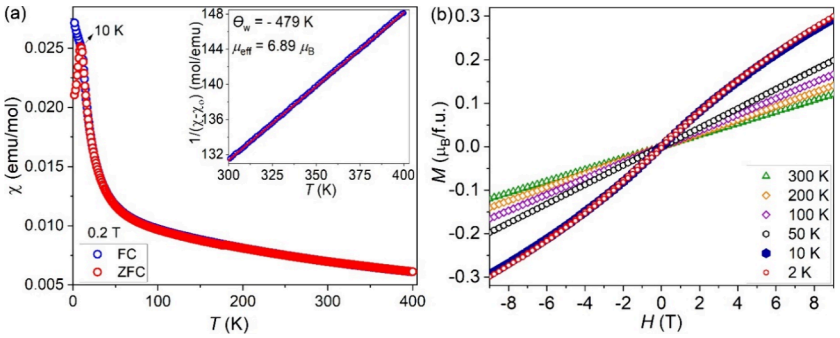

Figure 9. (a) ZFC-FC magnetic susceptibility with a magnetic field of 0.2 T with inverse FC magnetic susceptibility fit of $Ba_4RuMn_2O_{10}$ with the $1/(\chi - \chi_0) = (T - \Theta_w)/C$ equation (inset) and (b) isothermal-field-dependent magnetization of $Ba_4RuMn_2O_{10}$ between 2 and 300 K (inset).

with $\mu_{eff}(Ru^{4+}) = 4.9\ \mu_B$ and $\mu_{eff}(Mn^{4+}) = 3.87\ \mu_B$. The calculation of the frustration factor (f) with the formula $f = |\Theta_w|/T_f$ yields $f = 48$, which indicates the existence of strong magnetic frustration that could be related to the disordered Ru/Mn site in the trimers.

The low-temperature neutron diffraction data were collected, but no additional scattering associated with the long-range magnetic ordering was detected (Figure S5), suggesting strongly fluctuating moments of a glassy magnetic ground state. The magnetic behavior of $Ba_4RuMn_2O_{10}$ is different from the long-range antiferromagnetic (AFM) ordering observed in the parent compounds, $Ba_4Ru_3O_{10}$ and $Ba_4Mn_3O_{10}$, which shows a Néel temperature (T_N) at ∼105 and ∼40−80 K, respectively.[12,19,42,43] In the magnetic structure of $Ba_4Ru_3O_{10}$, only Ru2 sites (Ru atoms at the end of the trimer) order magnetically with ∼1 μ_B in an antiparallel arrangement (Ru1 site remains paramagnetic), while all Mn atoms are ordered with a larger magnitude of moment (2.23 and −1.98 μ_B) in the $Ba_4Mn_3O_{10}$ compound.[12,43] If we assume there are AFM states in $Ba_4RuMn_2O_{10}$ adopting the magnetic structure of parent compounds in such a polar crystal structure (Figure S6), fitting the 1.7 K data with adapted models yields reduced ordered moments per mixed Mn/Ru site of 0.4(1) μ_B (Figure S7). This moment represents our detection limit defined by our experimental error bars.

To confirm the spin-glass behavior, AC magnetic susceptibility measurements were carried out at four different frequencies (1, 10, 100, and 1000 Hz), showing typical frequency-dependent maxima near the spin-freezing transition temperature (Figure 10). The empirical Mydosh parameter (φ) can be calculated based on $\varphi = (T_{max}(\nu_1) - T_{max}(\nu_2))/(T_{max}(\nu_1) \times (\log \nu_1 - \log \nu_2))$, where the $T_{max}(\nu)$ is the temperature corresponding to the maxima in the AC magnetic susceptibility at the frequency of ν. The calculated φ is 0.032(1), which is within the typical range (0.004−0.08) of spin glasses.[44] The spin glass behavior is probably due to the disordered metal sites and strong magnetic frustration in this system.

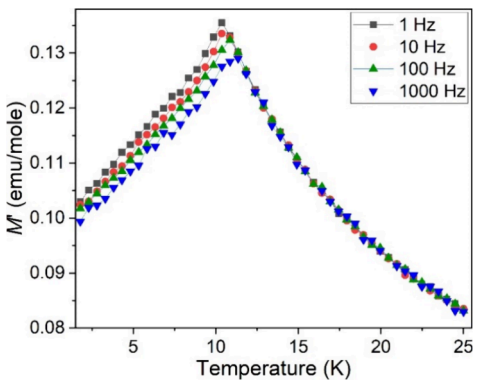

Figure 10. AC magnetic susceptibility data of $Ba_4RuMn_2O_{10}$.

Heat capacity (C_P) measurements were conducted on a dense pellet of $Ba_4RuMn_2O_{10}$ from 1.8 to 50 K under 0 T (Figure 11). The absence of a typical λ-like anomaly supports the lack of long-range magnetic ordering. The heat capacity C_P has both electron ($C_e = \gamma T$) and lattice contribution ($C_l = \beta T^3 + \alpha T^5$). For this compound (not metallic as shown below), the C_l is much larger than C_e, and C_P requires three terms in the modified Debye model ($C_P/T = \gamma + \beta T^2 + \alpha T^4$) to fit the low-temperature range (1.8−5 K), which yields the Sommerfeld coefficient γ (21 mJ/(mol·K^2)) and coefficient β (5.67×10^{-3} J/(mol·K^4)). The obtained γ (21 mJ/(mol·K^2)) is comparable with the value obtained in the related compound $Ba_4Ir_3O_{10}$, which also lacks the long-range magnetic order but shows strong AFM exchange interactions.[45] The coefficient β is associated with the Debye temperature (Θ_D) as $\Theta_D^3 = 12\pi^4 Rn/(5\beta)$, where $R = 8.314$ J/(mol·K), $n = 17$ (the number of atoms per formula unit), and the Θ_D is determined to be 180 K, which is smaller than that (400 K) of $Ba_4Mn_3O_{10}$.[46]

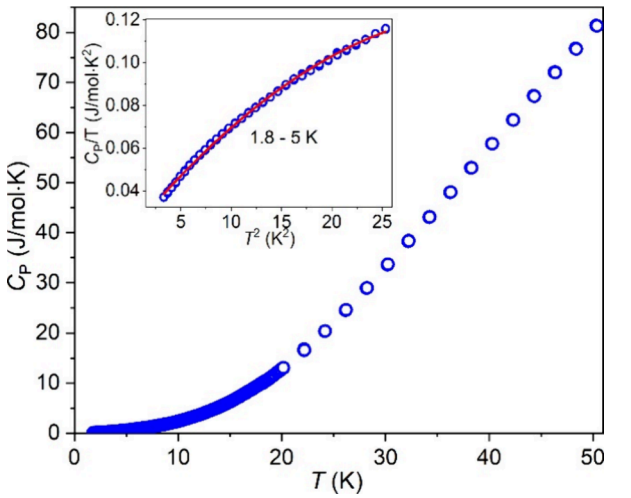

Figure 11. Heat capacity C_P measured from 1.8 to 50 K (the low-temperature range) fitting with the modified Debye model $C_P/T = \gamma + \beta T^2 + \alpha T^4$ (inset).

Resistivity measured as a function of temperature (300−1373 K) indicates that it is a semiconductor. The bandgap (E_g)

https://doi.org/10.1021/acs.chemmater.4c00586
Chem. Mater. 2024, 36, 6053−6061

can be estimated via the formula of $E_g \sim 2E_a$ (thermal activation energy) and the fitting of the data with the Arrhenius equation $\ln \rho = \ln \rho_0 + E_a/k_BT$, where ρ_0 is the pre-exponential factor and k_B is the Boltzmann constant (Figure 12). Based on the obtained value of E_a, the E_g is estimated to be ~0.6 eV, which is close to those theoretical values of $Ba_4Ru_3O_{10}$.[47,48]

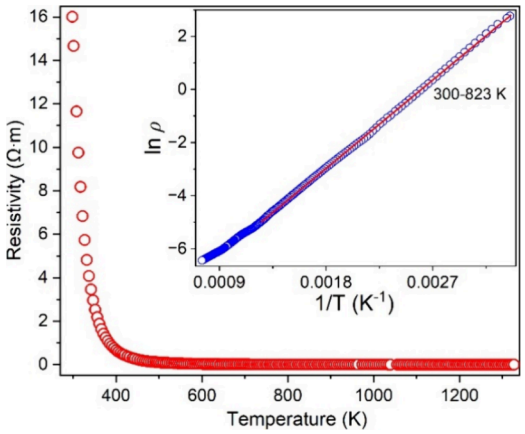

Figure 12. Temperature-dependent resistivity of $Ba_4RuMn_2O_{10}$ with a plot of ln ρ vs $1/T$ with the linear fitting of the data (300−823 K) using the Arrhenius equation $\ln \rho = \ln \rho_0 + E_a/k_BT$.

CONCLUSION

In summary, phase-pure polycrystalline $Ba_4RuMn_2O_{10}$ can be successfully prepared via the high-temperature solid-state method. The NCS polar space group was confirmed by SHG, CBED, and HAADF-STEM. Rietveld refinements using PND data proved the three partially disordered Ru/Mn sites with different ratios of Ru:Mn. XANES confirms the +4 valence state of Ru/Mn. $Ba_4RuMn_2O_{10}$ exhibits semiconducting behavior with a narrow bandgap and spin-glass state. The design strategy of converting the CS $Ba_4T_3O_{10}$ (T = Mn, Ru) into NCS polar $Ba_4RuMn_2O_{10}$ via creating three unevenly distorted octahedra in the trimers with partially disordered Ru/Mn metal sites is successful. This method may be applied to prepare $Ba_4Ru_{3-x}Mn_xO_{10}$ ($0 < x < 3$) and other novel compounds based on $Ba_4T_3O_{10}$ (T = Mn, Ru, Ir) parent compounds and similar CS crystal structures featuring trimers or pentamers.

ASSOCIATED CONTENT

Supporting Information

The Supporting Information is available free of charge at https://pubs.acs.org/doi/10.1021/acs.chemmater.4c00586.

XRD patterns at low angles; EDX elemental maps; Ru-K edges of $Ba_4RuMn_2O_{10}$; ZFC-FC data at 0.1 T; PND patterns of $Ba_4RuMn_2O_{10}$ at 1.7 and 250 K; magnetic structures of the parent compounds redefined for the polar symmetry of $Ba_4RuMn_2O_{10}$; the refined neutron data of $Ba_4RuMn_2O_{10}$ measured at 1.7 K (PDF)

AUTHOR INFORMATION

Corresponding Author

Xiaoyan Tan − *Department of Chemistry and Biochemistry, George Mason University, Fairfax, Virginia 22030, United States; Quantum Science and Engineering Center, George Mason University, Fairfax, Virginia 22030, United States;* orcid.org/0000-0002-1742-8252; Email: xtan6@gmu.edu

Authors

Callista M. Skaggs − *Department of Chemistry and Biochemistry, George Mason University, Fairfax, Virginia 22030, United States*

Peter E. Siegfried − *Department of Physics and Astronomy and Quantum Science and Engineering Center, George Mason University, Fairfax, Virginia 22030, United States;* orcid.org/0000-0002-0145-2899

Jun Sang Cho − *Department of Physics, Sogang University, Seoul 04017, Republic of Korea*

Yan Xin − *National High Magnetic Field Laboratory, Florida State University, Tallahassee, Florida 32310, United States*

V. Ovidiu Garlea − *Neutron Scattering Division, Oak Ridge National Laboratory, Oak Ridge, Tennessee 37831, United States*

Keith M. Taddei − *Neutron Scattering Division, Oak Ridge National Laboratory, Oak Ridge, Tennessee 37831, United States; X-ray Science Division, Advanced Photon Source, Argonne National Laboratory, Lemont, Illinois 60439, United States*

Hari Bhandari − *Department of Physics and Astronomy, George Mason University, Fairfax, Virginia 22030, United States; Department of Physics and Astronomy and Stavropoulos Center for Complex Quantum Matter, University of Notre Dame, Notre Dame, Indiana 46556, United States*

Mark Croft − *Department of Physics and Astronomy, Rutgers, The State University of New Jersey, Piscataway, New Jersey 08854, United States*

Nirmal J. Ghimire − *Department of Physics and Astronomy and Stavropoulos Center for Complex Quantum Matter, University of Notre Dame, Notre Dame, Indiana 46556, United States*

Joon I. Jang − *Department of Physics, Sogang University, Seoul 04017, Republic of Korea;* orcid.org/0000-0002-1608-8321

Complete contact information is available at: https://pubs.acs.org/10.1021/acs.chemmater.4c00586

Notes

The authors declare no competing financial interest.

ACKNOWLEDGMENTS

C.M.S. and X.T. were supported by start-up funding from George Mason University. J.I.J. acknowledges support from the Basic Science Research Programs (2021R1A2C2013625) and Basic Research Laboratory Program (2022R1A4A1033562) through the National Research Foundation of Korea (NRF), funded by the Korean government. N.J.G acknowledges the support from the National Science Foundation (NSF) CAREER award DMR-2143903. TEM work was performed at the National High Magnetic Field Laboratory, which is supported by the National Science Foundation Cooperative Agreement No. DMR-1644779, DMR-2128556, and the State of Florida. This research used resources at the High Flux Isotope Reactor, a DOE Office of Science User Facilities operated by the Oak Ridge National Laboratory.

REFERENCES

(1) Halasyamani, P. S.; Poeppelmeier, K. R. Noncentrosymmetric Oxides. *Chem. Mater.* **1998**, *10*, 2753−2769.
(2) Zhang, Y.; Xie, M.; Adamaki, V.; Khanbareh, H.; Bowen, C. R. Control of Electro-Chemical Processes Using Energy Harvesting Materials and Devices. *Chem. Soc. Rev.* **2017**, *46*, 7757−7786.
(3) Nan, C. W.; Bichurin, M. I.; Dong, S.; Viehland, D.; Srinivasan, G. Multiferroic Magnetoelectric Composites: Historical Perspective, Status, and Future Directions. *J. Appl. Phys.* **2008**, *103*, 031101.
(4) Meisenheimer, P.; Zhang, H.; Raftrey, D.; Chen, X.; Shao, Y. T.; Chan, Y. T.; Yalisove, R.; Chen, R.; Yao, J.; Scott, M. C.; Wu, W.; Muller, D. A.; Fischer, P.; Birgeneau, R. J.; Ramesh, R. Ordering of Room-Temperature Magnetic Skyrmions in a Polar van Der Waals Magnet. *Nat. Commun.* **2023**, *14*, 3744.
(5) Shiv Halasyamani, P. Polar Inorganic Materials: Opportunities and Challenges. *J. Solid State Chem.* **2012**, *195*, 1.
(6) Bennett, J. W.; Rabe, K. M. Searches for New Ferroelectrics: Strategies and Explorations. *J. Solid State Chem.* **2012**, *195*, 21−31.
(7) Huai, X.; Tran, T. T. Design Principles for Noncentrosymmetric Materials. *Annu. Rev. Mater. Res.* **2023**, *53*, 253−274.
(8) Zagorac, D.; Muller, H.; Ruehl, S.; Zagorac, J.; Rehme, S. Recent Developments in the Inorganic Crystal Structure Database: Theoretical Crystal Structure Data and Related Features. *J. Appl. Crystallogr.* **2019**, *52*, 918−925.
(9) Shi, Y.; Guo, Y.; Wang, X.; Princep, A. J.; Khalyavin, D.; Manuel, P.; Michiue, Y.; Sato, A.; Tsuda, K.; Yu, S.; et al. A Ferroelectric-like Structural Transition in a Metal. *Nat. Mater.* **2013**, *12*, 1024−1027.
(10) Sharma, I. B.; Singh, D. Solid State Chemistry of Ruddlesden-Popper Type Complex Oxides. *Bull. Mater. Sci.* **1998**, *21*, 363−374.
(11) Carim, A. H.; Dera, P.; Finger, L. W.; Mysen, B.; Prewitt, C. T.; Schlom, D. G. Crystal Structure and Compressibility of $Ba_4Ru_3O_{10}$. *J. Solid State Chem.* **2000**, *149*, 137−142.
(12) Zubkov, V. G.; Tyutyunnik, A. P.; Berger, I. F.; Voronin, V. I.; Bazuev, G. V.; Moore, C. A.; Battle, P. D. Crystal and Magnetic Structures of $Ba_4Mn_3O_{10}$. *J. Solid State Chem.* **2002**, *167*, 453−458.
(13) Cao, G.; Zheng, H.; Zhao, H.; Ni, Y.; Pocs, C. A.; Zhang, Y.; Ye, F.; Hoffmann, C.; Wang, X.; Lee, M.; Hermele, M.; Kimchi, I. Quantum Liquid from Strange Frustration in the Trimer Magnet $Ba_4Ir_3O_{10}$. *npj Quantum Mater.* **2020**, *5*, 26.
(14) Chen, R.; Greenblatt, M.; Bendersky, L. A. Stabilization of the n = 3 Ruddlesden-Popper Phases: $Sr_4Mn_{3-x}Fe_xO_{10-\delta}$ and $Sr_{4-y}Ca_yMn_3O_{10-\delta}$. *Chem. Mater.* **2001**, *13*, 4094−4100.
(15) Neubacher, M.; Müller-Buschbaum, H. A New Oxoruthenate (IV): $Ba_4Ru_{1.1}Mn_{1.9}O_{10}$ with Statistically Occupied M^{4+} Positions. *Monatshefte für Chemie Chem. Mon.* **1990**, *121*, 635−640.
(16) Garlea, V. O.; Chakoumakos, B. C.; Moore, S. A.; Taylor, G. B.; Chae, T.; Maples, R. G.; Riedel, R. A.; Lynn, G. W.; Selby, D. L. The High-Resolution Powder Diffractometer at the High Flux Isotope Reactor. *Appl. Phys. A Mater. Sci. Process.* **2010**, *99*, 531−535.
(17) Calder, S.; An, K.; Boehler, R.; Dela Cruz, C. R.; Frontzek, M. D.; Guthrie, M.; Haberl, B.; Huq, A.; Kimber, S. A. J.; Liu, J.; Molaison, J. J.; Neuefeind, J.; Page, K.; dos Santos, A. M.; Taddei, K. M.; Tulk, C.; Tucker, M. G. A Suite-Level Review of the Neutron Powder Diffraction Instruments at Oak Ridge National Laboratory. *Rev. Sci. Instrum.* **2018**, *89*, 092701.
(18) Rodriguez-Carvajal, J. Recent Advances in Magnetic Structure Determination by Neutron Powder Diffraction. *Phys. B Condens. Matter* **1993**, *192*, 55−69.
(19) Sannigrahi, J.; Chattopadhyay, S.; Bhattacharyya, A.; Giri, S.; Majumdar, S.; Venkateshwarlu, D.; Ganesan, V. Two Dimensional Magnetic Correlation in the Unconventional Corrugated Layered Oxides $(Ba,Sr)_4Mn_3O_{10}$. *J. Phys.: Condens. Matter* **2015**, *27*, 056001.
(20) Williams, D. B.; Carter, C. B. *Transmission Electron Microscopy: A Textbook for Materials Science*; Plenum Press: New York, 1996.
(21) Pennycook, S. J.; Boatner, L. A. Chemically Sensitive Structure-Imaging with a Scanning Transmission Electron Microscope. *Nature* **1988**, *336*, 565−567.
(22) Carim, A. H.; Dera, P.; Finger, L. W.; Mysen, B.; Prewitt, C. T.; Schlom, D. G. Crystal Structure and Compressibility of $Ba_4Ru_3O_{10}$. *J. Solid State Chem.* **2000**, *149*, 137−142.
(23) Vasala, S.; Karppinen, M. $A_2B'B''O_6$ Perovskites: A Review. *Prog. Solid State Chem.* **2015**, *43*, 1−36.
(24) Shannon, R. D. Revised Effective Ionic Radii and Systematic Studies of Interatomic Distances in Halides and Chalcogenides. *Acta Crystallogr.* **1976**, *A32*, 751−767.
(25) Puggioni, D.; Rondinelli, J. M. Designing a Robustly Metallic Noncenstrosymmetric Ruthenate Oxide with Large Thermopower Anisotropy. *Nat. Commun.* **2014**, *5*, 3432.
(26) Giovannetti, G.; Puggioni, D.; Rondinelli, J. M.; Capone, M. Interplay between Electron Correlations and Polar Displacements in Metallic $SrEuMo_2O_6$. *Phys. Rev. B* **2016**, *93*, 115147.
(27) Cai, G. H.; Greenblatt, M.; Li, M. R. Polar Magnets in Double Corundum Oxides. *Chem. Mater.* **2017**, *29*, 5447−5457.
(28) Feng, H. L.; Kang, C. J.; Kim, B.; Kim, K.; Croft, M.; Liu, S.; Tyson, T. A.; Stavitski, E.; Zu, R.; Gopalan, V.; et al. A Polar Magnetic and Insulating Double Corundum Oxide: Mn_2MnSbO_6 with Ordered Mn(II) and Mn(III) Ions. *Chem. Mater.* **2021**, *33*, 6522−6529.
(29) Shaikh, M.; Fathima, A.; Swamynadhan, M. J.; Das, H.; Ghosh, S. Investigation into Cation-Ordered Magnetic Polar Double Perovskite Oxides. *Chem. Mater.* **2021**, *33*, 1594−1606.
(30) Maunders, C.; Etheridge, J.; Wright, N.; Whitfield, H. J. Structure and Microstructure of Hexagonal $Ba_3Ti_2RuO_9$ by Electron Diffraction and Microscopy. *Acta Crystallogr. Sect. B Struct. Sci.* **2005**, *61*, 154−159.
(31) Radtke, G.; Maunders, C.; Saúl, A.; Lazar, S.; Whitfield, H. J.; Etheridge, J.; Botton, G. A. Electronic Structure and Stability of Hexagonal $Ba_3Ti_2RuO_9$. *Phys. Rev. B - Condens. Matter Mater. Phys.* **2010**, *81*, 085112.
(32) Zhou, H. D.; Choi, E. S.; Li, G.; Balicas, L.; Wiebe, C. R.; Qiu, Y.; Copley, J. R. D.; Gardner, J. S. Spin Liquid State in the S = 1/2 Triangular Lattice $Ba_3CuSb_2O_9$. *Phys. Rev. Lett.* **2011**, *106*, 147204.
(33) Ferreira, T.; Carone, D.; Huon, A.; Herklotz, A.; Stoian, S. A.; Heald, S. M.; Morrison, G.; Smith, M. D.; Loye, H. C. z. $Ba_3Fe_{1.56}Ir_{1.44}O_9$: A Polar Semiconducting Triple Perovskite with Near Room Temperature Magnetic Ordering. *Inorg. Chem.* **2018**, *57*, 7362−7371.
(34) Sakamoto, T.; Doi, Y.; Hinatsu, Y. Crystal Structures and Magnetic Properties of 6H-Perovskite-Type Oxides $Ba_3MIr_2O_9$ (M = Mg, Ca, Sc, Ti, Zn, Sr, Zr, Cd and In). *J. Solid State Chem.* **2006**, *179*, 2595−2601.
(35) Dey, T.; Mahajan, A. V.; Khuntia, P.; Baenitz, M.; Koteswararao, B.; Chou, F. C. Spin-Liquid Behavior in J_{eff}=1/2 Triangular Lattice Compound $Ba_3IrTi_2O_9$. *Phys. Rev. B - Condens. Matter Mater. Phys.* **2012**, *86*, 140405.
(36) Altermatt, D.; Brown, I. D. The Automatic Searching for Chemical Bonds in Inorganic Crystal Structures. *Acta Crystallogr.* **1985**, *B41*, 240−244.
(37) Croft, M.; Sills, D.; Greenblatt, M.; Lee, C.; Cheong, S.-W.; Ramanujachary, K. V.; Tran, D. Systematic Mn d-Configuration Change in the $La_{1-x}Ca_xMnO_3$ System: A Mn K-Edge XAS Study. *Phys. Rev. B - Condens. Matter Mater. Phys.* **1997**, *55*, 8726−8732.
(38) Mandal, T. K.; Croft, M.; Hadermann, J.; Van Tendeloo, G.; Stephens, P. W.; Greenblatt, M. La_2MnVO_6 Double Perovskite: A Structural, Magnetic and X-Ray Absorption Investigation. *J. Mater. Chem.* **2009**, *19*, 4382−4390.
(39) Mandal, T. K.; Abakumov, A. M.; Hadermann, J.; Van Tendeloo, G.; Croft, M.; Greenblatt, M. Synthesis, Crystal Structure, and Magnetic Properties of $Sr_{1.31}Co_{0.63}Mn_{0.37}O_3$: A Derivative of the Incommensurate Composite Hexagonal Perovskite Structure. *Chem. Mater.* **2007**, *19*, 6158−6167.
(40) Deng, Z.; Retuerto, M.; Liu, S.; Croft, M.; Stephens, P. W.; Calder, S.; Li, W.; Chen, B.; Jin, C.; Hu, Z.; Li, M.-R.; Lin, H.-J.; Chan, T.-S.; Chen, C.-T.; Kim, S. W.; Greenblatt, M. Dynamic Ferrimagnetic Order in a Highly Distorted Double Perovskite Y_2CoRuO_6. *Chem. Mater.* **2018**, *30*, 7047−7054.

https://doi.org/10.1021/acs.chemmater.4c00586
Chem. Mater. 2024, 36, 6053−6061

(41) Bune, R. O.; Lobanov, M. V.; Popov, G.; Greenblatt, M.; Botez, C. E.; Stephens, P. W.; Croft, M.; Hadermann, J.; Van Tendeloo, G. Crystal Structure and Properties of Ru-Stoichiometric $LaSrMnRuO_6$. *Chem. Mater.* **2006**, *18*, 2611−2617.
(42) Souda, N.; Zhang, W.; Sakurai, T.; Okubo, S.; Ohta, H.; Nishimura, K.; Sakurai, H.; Yoshimura, K.; Takayama-Muromachi, E. High Field ESR Studies of Layered Manganese Oxides $A_4Mn_3O_{10}$ (A = Ba, Sr). *J. Magn. Magn. Mater.* **2007**, *310*, 1829−1831.
(43) Klein, Y.; Rousse, G.; Damay, F.; Porcher, F.; André, G.; Terasaki, I. Antiferromagnetic Order and Consequences on the Transport Properties of $Ba_4Ru_3O_{10}$. *Phys. Rev. B - Condens. Matter Mater. Phys.* **2011**, *84*, 054439.
(44) Mydosh, J. A. *Spin Glasses: An Experimental Introduction*; Taylor & Francis: Washington, DC, 1993.
(45) Cao, G.; Zheng, H.; Zhao, H.; Ni, Y.; Pocs, C. A.; Zhang, Y.; Ye, F.; Hoffmann, C.; Wang, X.; Lee, M.; Hermele, M.; Kimchi, I. Quantum Liquid from Strange Frustration in the Trimer Magnet $Ba_4Ir_3O_{10}$. *npj Quantum Mater.* **2020**, *5*, 1−7.
(46) Sannigrahi, J.; Chattopadhyay, S.; Bhattacharyya, A.; Giri, S.; Majumdar, S.; Venkateshwarlu, D.; Ganesan, V. Two Dimensional Magnetic Correlation in the Unconventional Corrugated Layered Oxides $(Ba,Sr)_4Mn_3O_{10}$. *J. Phys.: Condens. Matter* **2015**, *27*, 056001.
(47) Streltsov, S. V.; Khomskii, D. I. Unconventional Magnetism as a Consequence of the Charge Disproportionation and the Molecular Orbital Formation in $Ba_4Ru_3O_{10}$. *Phys. Rev. B - Condens. Matter Mater. Phys.* **2012**, *86*, 064429.
(48) Radtke, G.; Saúl, A.; Klein, Y.; Rousse, G. Magnetism of $Ba_4Ru_3O_{10}$ Revealed by Density Functional Calculations: Structural Trimers Behaving as Coupled Magnetic Dimers. *Phys. Rev. B - Condens. Matter Mater. Phys.* **2013**, *87*, 054436.

https://doi.org/10.1021/acs.chemmater.4c00586
Chem. Mater. 2024, 36, 6053−6061